GEOPHYSICS, VOL. 78, NO. 1 (JANUARY-FEBRUARY 2013); P. C11–C23, 18 FIGS., 1 TABLE.
10.1190/GEO2012-0066.1

Ray-based gridded tomography for tilted transversely isotropic media

Xiaoxiang Wang[1] and Ilya Tsvankin[2]

ABSTRACT

Reflection tomography in the migrated domain can help reconstruct heterogeneous, anisotropic velocity fields needed for accurate depth imaging of complex geologic structures. The presence of anisotropy, however, increases the uncertainty in velocity analysis and typically requires a priori constraints on the model parameters. Here, we develop a 2D P-wave tomographic algorithm for heterogeneous transversely isotropic media with a tilted symmetry axis (TTI) and investigate the conditions necessary for stable estimation of the symmetry-direction velocity V_{P0} and the anisotropy parameters ε and δ. The model is divided into rectangular cells, and the parameters V_{P0}, ε, δ, and the tilt ν of the symmetry axis are defined at the grid points. To increase the stability of the inversion, the symmetry axis is set orthogonal to the imaged reflectors, with the tilt interpolated inside each layer. The iterative migration velocity analysis involves efficient linearized parameter updating designed to minimize the residual moveout in image gathers for all available reflection events. The moveout equation in the depth-migrated domain includes a nonhyperbolic term that describes long-offset data, which are particularly sensitive to ε. Synthetic tests for models with a "quasi-factorized" TTI syncline (i.e., ε and δ are constant inside the anisotropic layer) and a TTI thrust sheet demonstrate that stable parameter estimation requires either strong smoothness constraints or additional information from walkaway VSP (vertical seismic profiling) traveltimes. If the model is quasi-factorized with a linear spatial variation of V_{P0}, it may be possible to obtain the interval TTI parameters just from long-spread reflection data.

INTRODUCTION

Prestack depth migration, or PSDM (e.g., Berkhout, 1982; Etgen, 1988; Lumley, 1989) has become the most widely used imaging technique in seismic exploration because of its high accuracy for complex subsurface structures. Velocity models for depth imaging are usually built by migration velocity analysis (MVA), which operates in the migrated domain (Fowler, 1988; Deregowski, 1990; Etgen, 1990; van Trier, 1990; Liu, 1997).

The goal of MVA is to remove residual moveout of reflection events in common-image gathers (CIGs), obtained by computing migrated depth as a function of offset. Due to the high sensitivity of CIGs to medium parameters, quantitative analysis of the relationship between the residual moveout and velocity field helps refine the model, usually in iterative fashion. However, the flatness of CIGs is a necessary, but not a sufficient condition for resolving the medium parameters. Therefore, velocity model-building using CIGs typically requires additional constraints (e.g., well measurements) to reduce the nonuniqueness of the inverse problem.

Since most subsurface formations are anisotropic, ignoring anisotropy in P-wave processing leads to image distortions and interpretation errors (e.g., Alkhalifah and Larner, 1994; Alkhalifah et al., 1996; Vestrum et al., 1999). For example, in complex geologic settings including fold-and-thrust belts and subsalt plays, sedimentary formations are often described by transversely isotropic models with a vertical (VTI) or tilted (TTI) symmetry axis (Douma et al., 2009; Neal et al., 2009; Bakulin et al., 2010a). To ensure stable estimation of the symmetry-direction P-wave velocity V_{P0} and anisotropy parameters ε and δ, the orientation of the symmetry axis is commonly assumed to be known from structural information (Audebert et al., 2006; Bakulin et al., 2010b).

Behera and Tsvankin (2009) develop a 2D MVA algorithm for heterogeneous TTI media based on the approach suggested by Sarkar and Tsvankin (2004) for vertical transverse isotropy. To reduce the number of unknown parameters, they divide the model into

Manuscript received by the Editor 24 February 2012; revised manuscript received 14 August 2012; published online 4 January 2013.
[1]Formerly Colorado School of Mines, Center for Wave Phenomena, Geophysics Department, Golden, Colorado, USA; presently Shell Exploration & Production Company, New Orleans, Louisiana, USA. E-mail: xiaoxiang.wang@shell.com.
[2]Colorado School of Mines, Center for Wave Phenomena, Geophysics Department, Golden, Colorado, USA. E-mail: ilya@dix.mines.edu.

quasi-factorized TTI blocks. Within each block, the parameters ε and δ are constant, and the symmetry-direction velocity V_{P0} varies linearly according to the vertical (k_z) and lateral (k_x) gradients. Behera and Tsvankin (2009) also adopt the widely used assumption that the symmetry axis is perpendicular to the bottom of TTI layers (i.e., the tilt ν of the symmetry axis is equal to the reflector dip). They show that the gradients k_z and k_x and the parameters ε and δ can be accurately resolved, if V_{P0} is specified at a single point in each block. Note that stable estimation of ε in TTI media requires long-spread (nonhyperbolic) moveout with the maximum offset reaching at least two reflector depths. Despite the efficiency of Behera and Tsvankin's (2009) algorithm, their relatively simple model representation may be inadequate for complex subsurface structures with nonlinear spatial parameter variations.

To handle realistic subsurface geology, the model can be divided into relatively small cells, and the parameters at each grid point are often estimated using ray-based postmigration tomography (Stork, 1992; Campbell et al., 2006; Woodward et al., 2008). Most current applications of gridded tomography to TTI media simplify the inversion by keeping ε and δ fixed and updating only the symmetry-direction velocity V_{P0} (Charles et al., 2008; Huang et al., 2008). This procedure, however, does not adequately describe anisotropic velocity fields and may distort NMO velocities for both horizontal and dipping events. Zhou et al. (2011) develop multiparameter tomography for TTI media and apply it to field data. They find that simultaneous estimation of all three relevant parameters (V_{P0}, ε, and δ) provides a better data fit than single-parameter (only velocity) inversion. Zhou et al. (2011) also conclude that trade-offs between the TTI parameters cannot be eliminated using only P-wave reflections, and point out the importance of additional constraints from well data. However, they do not carry out joint inversion of reflection and borehole data including, for example, VSP (vertical seismic profiling) traveltimes.

Bakulin et al. (2010b) develop localized gridded anisotropic tomography, which combines surface seismic data with borehole measurements (acoustic logs or check-shot surveys). Despite the additional constraints, they still obtain a wide range of TTI models that flatten the CIGs and fit the borehole data. The nonuniqueness may be partially caused by the limited angle coverage of check-shot rays. Bakulin et al. (2010b) also use a constant (45°) tilt of the symmetry axis for their synthetic model, not a practical assumption for field data.

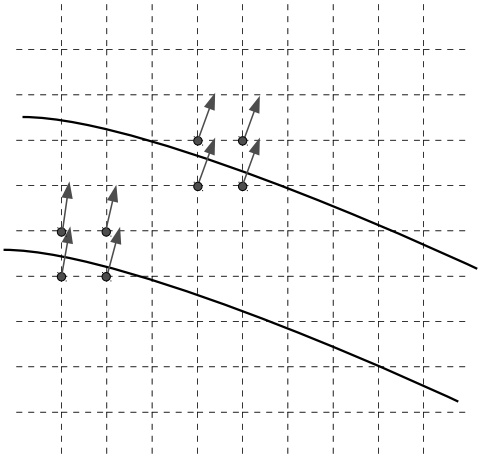

Figure 1. Gridded model (dashed lines) used in MVA. The symmetry axis (arrows) at the vertices (dots) of each cell crossed by an interface (solid lines) is set orthogonal to the corresponding interface segment.

Here, we present a 2D ray-based tomographic algorithm designed to iteratively update TTI parameters defined on rectangular (in some cases square) grids. The symmetry axis is set perpendicular to the interfaces that may be dipping or curved. To construct the Fréchet matrix, which links the model update and the data misfit, the traveltime derivatives with respect to the parameters at each grid point are computed numerically along the ray trajectory. We test the algorithm on two synthetic models containing a TTI syncline and a thrust sheet. To better constrain the anisotropic velocity field, P-wave reflections are combined with walkaway VSP data by including the VSP traveltime misfit in the objective function.

METHODOLOGY

We start from an initial model, which can be built using conventional-spread P-wave reflection data combined with borehole information, such as check-shot traveltimes and reflector depths (Wang and Tsvankin, 2010). Then, the entire P-wave data volume is used to update the subsurface velocity field by flattening long-spread image gathers throughout the model. This linearized parameter update is implemented using the 2D ray-based gridded tomographic technique described below.

Input data

Images at each step of parameter updating are generated by 2D prestack Kirchhoff depth migration (Seismic Unix program "sukdmig2d"). The moveout of migrated events in CIGs serves as the input to the tomographic algorithm. To avoid manual moveout picking, MVA typically employs semblance analysis with an appropriate analytic representation of moveout as a function of offset. Conventionally, moveout in CIGs is described by the best-fit hyperbola with a single parameter (equivalent to NMO velocity) responsible for the term quadratic in the half-offset h. To constrain the TI anellipticity parameter η (and, therefore, ε), the hyperbolic approximation can be replaced by a more general nonhyperbolic equation (Sarkar and Tsvankin, 2004)

$$z^2(h) \approx z^2(0) + Rh^2 + S\frac{h^4}{h^2 + z^2(0)}, \qquad (1)$$

where z is migrated depth, and R and S are dimensionless coefficients used to estimate the magnitude of residual moveout. Alternatively, the residual moveout can be evaluated using nonparametric methods (e.g., Murphy and Gray, 1999).

Model representation

The model is divided into rectangular (sometimes square) cells (Figure 1), with the symmetry-direction velocity V_{P0} and the anisotropy parameters ε and δ defined at each vertex of the grid. The spatial variation of the model parameters inside each cell is obtained by 2D interpolation. The grid size is determined by the expected resolution, acquisition geometry, and subsurface structure. If the grid size is too large compared to the dimensions of geologic units, the property variation is oversimplified. On the other hand, if the grid is too fine, the parameters may be poorly constrained and

reside in the null space. Also, the grid size determines the number of unknown parameters and, therefore, influences the demands on computer memory.

When an interface crosses a cell, the symmetry axis at the four vertices of the cell is assumed to be orthogonal to the corresponding interface segment (Figure 1). Therefore, the tilt ν of the symmetry axis is taken equal to the interface dip ϕ calculated from the depth image. Then, the tilt field for the whole section is obtained by 2D linear interpolation.

Model updating

To update the velocity model, we extend to gridded TTI media the MVA algorithm of Sarkar and Tsvankin (2004) designed for piecewise-factorized VTI models. Because the number of unknowns in our model is much larger, the partial derivatives of traveltime with respect to the medium parameters cannot be obtained simply from traveltime differences caused by certain parameter perturbations (Sarkar and Tsvankin, 2004). Instead, the traveltime derivatives are found numerically along computed raypaths, as described below.

Suppose the number of grid points in the model is W, and there are N parameters defined at each grid point. Then we iteratively update the parameter vector $\boldsymbol{\lambda}$, which contains $W \times N$ elements, using the inversion algorithm introduced in Appendix A. Since the number of unknowns can be very large and the coverage of seismic rays for each cell is uneven, the tomographic inversion is generally ill-conditioned. Therefore, the inverse problem (equation A-4) should be constrained using regularization terms. To obtain the vector of model updates $\boldsymbol{\Delta\lambda}$, we minimize the following objective function (based on the L^2-norm):

$$\mathcal{F}(\boldsymbol{\Delta\lambda}) = \|\mathbf{A}\boldsymbol{\Delta\lambda} + \mathbf{b}\|^2 + \zeta_1^2 \|\boldsymbol{\Delta\lambda}\|^2 + \zeta_2^2 \|\mathbf{L}(\boldsymbol{\Delta\lambda} + \boldsymbol{\lambda}^{\mathbf{0}})\|^2, \tag{2}$$

where $\mathbf{A}$ is a matrix with $M \times P$ rows (M is the number of offsets in each CIG and P is the number of CIGs) and $W \times N$ columns whose elements are the derivatives of migrated depth with respect to the medium parameters, and $\mathbf{b}$ is a vector which contains the residual moveout of the migrated depths (see Appendix A). The matrix $\mathbf{L}$ is a finite-difference approximation of the Laplacian operator, which penalizes solutions that are rough in a second-derivative sense ($\boldsymbol{\lambda}^{\mathbf{0}}$ is the model obtained at the previous iteration), and ζ_2 is a regularization parameter that controls the trade-off between minimizing the data misfit and the norm of the model parameters scaled by $\mathbf{L}$. Also, the magnitudes of the parameter updates corresponding to small derivatives in the matrix $\mathbf{A}$ are governed by including the norm of $\boldsymbol{\Delta\lambda}$ with the weight ζ_1 in function 2.

Computation of traveltime derivatives

The matrix $\mathbf{A}$ contains the traveltime derivatives with respect to the medium parameters defined on grids (equation A-5). These derivatives can be computed numerically along each raypath (Jech and Pšenčík, 1992; Zhou et al., 2004; Zhou and Greenhalgh, 2008) using the first-order traveltime perturbation theory (Červený and Jech, 1982; Červený, 2001). The location of the imaged reflection point for each source-receiver pair (equation A-1) is obtained from the results of semblance analysis using equation 1. Then, starting from that reflection point, we use the initial-value ray-tracing algorithm of Alkhalifah (1995) for 2D TI media to search for the incidence and reflected ray trajectories that satisfy Snell's law and match the corresponding offset. The perturbation of the medium parameter $\delta\lambda_{is}$ on any raypath R causes the traveltime change $\delta\tau$ expressed to the first order by

$$\delta\tau = -\int_R \frac{1}{VV_G}\left(\frac{\partial V}{\partial \lambda_{is}}\right)\delta\lambda_{is}\,\mathrm{d}s, \tag{3}$$

where V and V_G are P-wave phase and group velocities, respectively, and $\mathrm{d}s$ is a small segment of R (denoted by the subscript s). Therefore, the traveltime derivative with respect to the parameter λ_i at a specific ray step is approximately given by

$$\frac{\partial\tau}{\partial\lambda_{is}} = -\frac{\delta t}{V}\left(\frac{\partial V}{\partial\lambda_{is}}\right), \tag{4}$$

where δt is the time sample (i.e., the traveltime along $\mathrm{d}s$) in ray tracing.

Next, we need to convert $\partial\tau/\partial\lambda_{is}$ into the derivative with respect to the parameter λ_{ic} at a grid point ($\partial\tau/\partial\lambda_{ic}$). If there are several time samples on a seismic ray inside one cell (Figure 2), the parameter perturbation for a specific time sample ($\delta\lambda_{is}$) can be obtained by Lagrange interpolation of the parameter perturbation at one vertex c (assuming the perturbations at the other three vertices $c+1$, $c+2$, and $c+3$ are all zero):

$$\delta\lambda_{is} = \delta\lambda_{ic}\prod_{d=1}^{3}\frac{\|\mathbf{x}_s - \mathbf{x}_{c+d}\|}{\|\mathbf{x}_c - \mathbf{x}_{c+d}\|}, \tag{5}$$

where $\mathbf{x}$ is the coordinate vector and $\|\ldots\|$ represents the distance between two points. Since the parameter perturbation at a grid point only influences the ray segments in the cells that have that grid point as a vertex, the traveltime derivative with respect to the parameter at the vertex c (in equation A-5) is

$$\frac{\partial\tau}{\partial\lambda_{ic}} = -\sum_{s=m}^{n}\left[\frac{\delta t}{V}\left(\frac{\partial V}{\partial\lambda_{is}}\right)\prod_{d=1}^{3}\frac{\|\mathbf{x}_s - \mathbf{x}_{c+d}\|}{\|\mathbf{x}_c - \mathbf{x}_{c+d}\|}\right]. \tag{6}$$

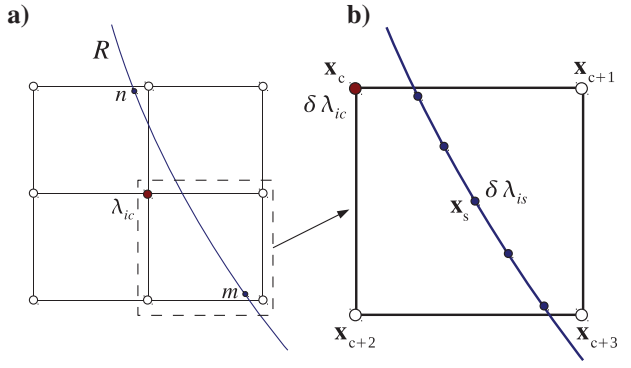

Figure 2. (a) Diagram of seismic ray R passing through three cells that share a grid point (in red); time samples along the ray change from m to n. (b) Enlarged cell with each time sample (ray step) marked in blue. The four vertices of the grid are defined by the coordinate vectors $\mathbf{x}_c$, $\mathbf{x}_{c+1}$, $\mathbf{x}_{c+2}$, and $\mathbf{x}_{c+3}$. The coordinate vector of a specific ray step is $\mathbf{x}_s$.

Here, the time samples along the ray passing through the cells that share the vertex c vary from m to n (Figure 2).

Finally, the problem reduces to the computation of the derivatives of the P-wave phase velocity V with respect to the medium parameters on the raypath. Using the P-wave phase-velocity function in TI media, the derivative $\partial V/\partial\lambda_{is}$ can be obtained analytically. The exact P-wave phase velocity in terms of the Thomsen parameters is given by Tsvankin (1996, 2005):

$$\frac{V^2}{V_{P0}^2} = 1 + \varepsilon\sin^2\theta - \frac{f}{2} + \frac{f}{2}\sqrt{\left(1+\frac{2\varepsilon\sin^2\theta}{f}\right)^2 - \frac{2(\varepsilon-\delta)\sin^2 2\theta}{f}}, \quad (7)$$

where θ is the phase angle with the symmetry axis, V_{P0} is the symmetry-direction velocity, and $f \equiv 1 - V_{S0}^2/V_{P0}^2$; V_{S0} is the symmetry-direction velocity of S-waves. Because the influence of V_{S0} on P-wave kinematics is negligible, the value of f can be set to a constant using a typical V_{P0}/V_{S0} ratio (e.g., $V_{P0}/V_{S0} = 2$).

The P-wave phase velocity can also be obtained from an approximation suggested by Fowler (2003) for VTI media:

$$2V^2 \approx V_h^2\sin^2\theta + V_{P0}^2\cos^2\theta + \sqrt{(V_h^2\sin^2\theta + V_{P0}^2\cos^2\theta)^2 + V_{P0}^2(V_{nmo}^2 - V_h^2)\sin^2 2\theta}, \quad (8)$$

where $V_h = V_{P0}\sqrt{1+2\varepsilon}$ is the velocity in the direction (horizontal in VTI media) perpendicular to the symmetry axis, and $V_{nmo} = V_{P0}\sqrt{1+2\delta}$ is the zero-dip NMO velocity. The advantage of equation 8 is that three velocity variables have the same units and similar magnitudes; therefore, all elements of $\mathbf{A}$ (equation 2) have the units of time. Moreover, equation 8 helps in constructing the regularization terms in equation 2. If the changes in ε and δ are small (e.g., $|\Delta\varepsilon| \le 0.02$; $|\Delta\delta| \le 0.02$), the updates of V_h and V_{nmo} can be converted into the updates of the Thomsen parameters via the relationships

$$\Delta V_h \approx V_{P0}\,\Delta\varepsilon; \qquad \Delta V_{nmo} \approx V_{P0}\,\Delta\delta. \quad (9)$$

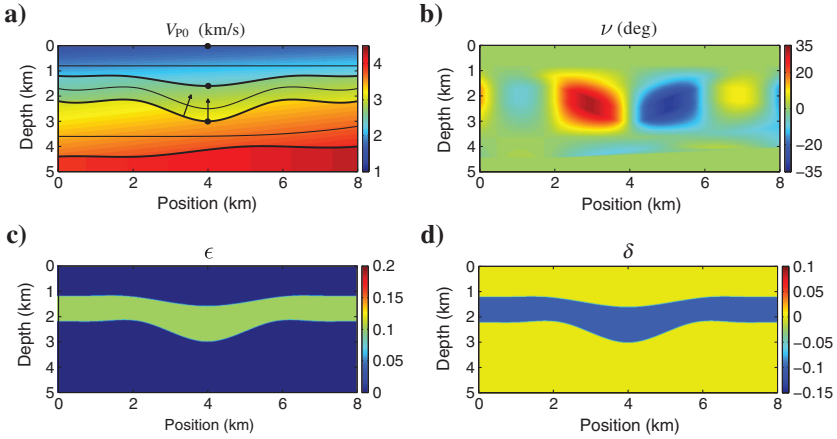

Figure 3. Model with a quasi-factorized TTI layer. (a) The layer boundaries are marked by bold black lines; within each layer, there is one more reflector (thin lines). The TTI layer in the middle is embedded between two isotropic layers. The symmetry-direction velocities at the top of each layer (at locations marked by three black dots in the middle of the model) are $V_{P0}^{(1)} = 1.62$ km/s, $V_{P0}^{(2)} = 2.66$ km/s, and $V_{P0}^{(3)} = 3.44$ km/s (from top to bottom). The velocity V_{P0} varies linearly in each layer according to the lateral gradients $k_x^{(1)} = 0.03$ s^{-1}, $k_x^{(2)} = 0.05$ s^{-1}, and $k_x^{(3)} = 0.05$ s^{-1}, and the vertical gradients $k_z^{(1)} = 0.5$ s^{-1}, $k_z^{(2)} = 0.4$ s^{-1}, and $k_z^{(3)} = 0.3$ s^{-1}. The symmetry axis (black arrows) is perpendicular to the boundaries of the TTI layer. (b) The field of the tilt angle ν of the symmetry axis with the vertical. (c, d) The anisotropy parameters ε and δ, which are constant in each layer ($\varepsilon^{(1)} = \delta^{(1)} = \varepsilon^{(3)} = \delta^{(3)} = 0$, $\varepsilon^{(2)} = 0.1$, and $\delta^{(2)} = -0.1$).

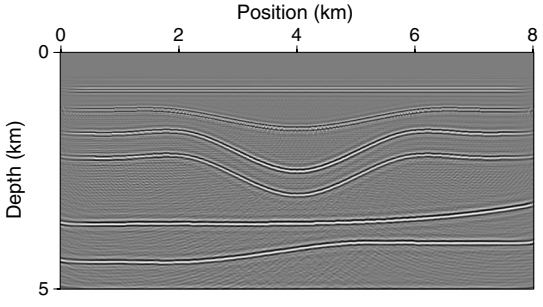

Figure 4. Depth image of the model from Figure 3 computed with the actual parameters.

SYNTHETIC EXAMPLES

Syncline model

Using a 2D finite difference program ("suea2df" in Seismic Unix), we generate P-wave reflection data for a medium similar to the syncline model of Behera and Tsvankin (2009) (Figure 3). A quasi-factorized TTI layer, with the boundaries dipping at angles up to 35° and the symmetry axis perpendicular to its bottom, is embedded between isotropic media. Each layer includes an additional reflector that helps estimate the vertical velocity gradient. The data are computed with shot and receiver intervals of 0.05 km; the maximum offset is 7 km. A depth section produced by Kirchhoff migration with the correct velocity model is shown in Figure 4; it is compared below with images generated using the inverted models. The artifacts are caused by noise in the synthetic data.

Test 1

In the first test, we assume that the first layer is known to be isotropic, while the other two layers are treated as quasi-factorized TTI. In each layer, the anisotropy parameters ε and δ are constant, and the symmetry-direction velocity V_{P0} is defined as

$$V_{P0}(x,z) = V_{P0}(x_0,z_0) + k_x(x-x_0) + k_z(z-z_0), \quad (10)$$

where $V_{P0}(x_0,z_0)$ is the value at a specific point (x_0,z_0); k_x and k_z are the lateral and vertical gradients, respectively. Thus, the model vector becomes

$$\boldsymbol{\lambda}_f = \{V_{P0}^{(n)},\, k_x^{(n)},\, k_z^{(n)},\, \varepsilon^{(n)},\, \delta^{(n)}\}, \qquad (n = 1,2,3), \quad (11)$$

where $V_{P0}^{(n)}$ is defined on top of each layer at the point with lateral coordinate $x_0 = 4$ km (Figure 3a); the depth $z_0^{(n)}$ of that point may change with the interface position after each iteration of MVA. Behera and Tsvankin (2009) assume that $V_{P0}^{(n)}$ is known at one point in each layer (e.g., from check shots) and demonstrate that the other elements of the model vector in equation 11 can be resolved by flattening CIGs of long-spread P-wave reflections.

The available range of dips in the TTI syncline, however, helps resolve the parameters V_{P0} and δ (Tsvankin and Grechka, 2011, section 2.4.1) in the second and third layer using just reflection traveltimes. Therefore, we relax the requirement of specifying the correct velocity value at a single location in each layer, and invert for $V_{P0}^{(n)}$. However, because the first layer is quasi-horizontal, $V_{P0}^{(1)}$ cannot be constrained without assuming isotropy (Behera and Tsvankin, 2009). Therefore, $\varepsilon^{(1)}$ and $\delta^{(1)}$ in the top layer are set to zero, with only $V_{P0}^{(1)}$, $k_x^{(1)}$, and $k_z^{(1)}$ estimated by MVA. The symmetry axis is assumed (correctly) to be perpendicular to the interfaces (see above), with the spatial distribution of the tilt ν between the interfaces obtained by linear interpolation.

The quasi-factorized assumption (which is valid for the model at hand) is equivalent to applying a strong smoothing constraint (described by the operator $\mathbf{L}$ in equation 2) to the anisotropic velocity field. Also, the number of unknown parameters (equation 11 with $\varepsilon^{(1)} = \delta^{(1)} = 0$) is significantly reduced.

The traveltime derivatives, however, are still calculated at the vertices of relatively small grids (equations 6 and 8). Therefore, we need to construct a mapping matrix $\mathbf{C}$ using the picked boundaries to convert the model update $\mathbf{\Delta\lambda}_f$ into the parameter perturbations ΔV_{P0}, ΔV_h, and ΔV_{nmo} at each grid point (equation 9; the grid size is 100 m × 100 m). Also, the updates at each iteration are constrained by $|\Delta V_{P0}^{(n)}| \le 0.05$ km/s, $\varepsilon^{(n)} \ge 0$, $|\Delta\varepsilon^{(n)}| \le 0.02$, and $|\Delta\delta^{(n)}| \le 0.02$, which corresponds to restricting the norm of model updates in equation 2. Therefore, without a regularization term, the inverse problem reduces to minimizing the function

$$\mathcal{F}(\mathbf{\Delta\lambda}_f) = \|\mathbf{AC}\,\mathbf{\Delta\lambda}_f + \mathbf{b}\|^2, \tag{12}$$

which can be accomplished by applying a linear least-squares algorithm (Gill et al., 1981; Coleman and Li, 1996).

Tomographic inversion is performed for 31 image gathers uniformly distributed between the horizontal coordinates 1 km and 7 km. The initial model used in the first iteration of MVA is composed of horizontal isotropic layers (Figure 5a). Because the velocity field is strongly distorted, the events exhibit significant residual moveout (Figure 5b) and the depth image is inaccurate (Figure 5c).

The inverted parameters after 20 iterations are listed in Table 1. As expected, the errors in the parameters of the third (deepest) layer are largest, primarily due to its smaller contribution to the effective reflection traveltimes. Also, because the two bottom reflectors have mild dips and the maximum offset-to-depth ratio for the deepest reflector is less than 1.5, the anisotropy parameters in the third layer are not well constrained. After PSDM, all CIGs become sufficiently flat (Figure 6a) with the maximum error in the migrated depth reaching 80 m for the bottom of the model (Figure 6b). If the correct values of $V_{P0}^{(n)}$ on top of each layer are used (as Behera and Tsvankin

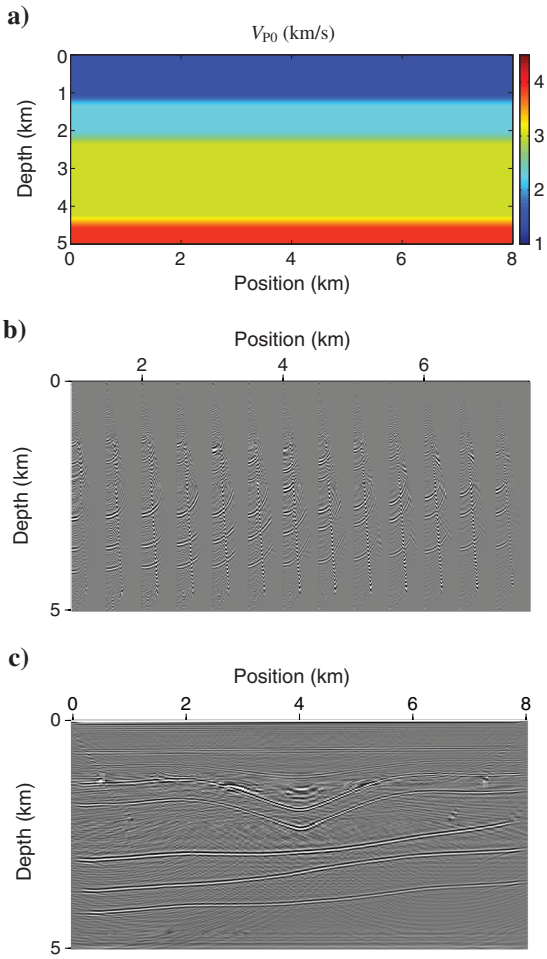

Figure 5. (a) Horizontally layered isotropic model used in the first iteration of velocity analysis. (b) CIGs (displayed every 0.5 km from 1 km to 7 km) after migration with the initial model. (c) The corresponding depth image. The bottom of the model is shifted up due to the inaccurate velocity field.

Table 1. Inversion results for test 1.

	V_{P0} (km/s)		k_x (s^{-1})		k_z (s^{-1})		ε		δ	
	Inverted	Error (%)	Inverted	Error	Inverted	Error	Inverted	Error	Inverted	Error
Layer 1	1.63	1	0.030	0	0.48	−0.02	—	—	—	—
Layer 2	2.63	−1	0.048	−0.002	0.43	0.03	0.10	0	−0.09	0.01
Layer 3	3.29	−4	0.046	−0.004	0.28	−0.02	0.05	0.05	0.05	0.05

[2009] did in their inversion), the velocity gradients and anisotropy parameters can be recovered with higher accuracy.

Test 2

This time, we relax the constraint on the spatial velocity variation, and update the symmetry-direction velocity V_{P0} at each grid point (the grid size is the same: 100 m × 100 m). The parameters ε and δ are still taken constant within each layer, as they are in the actual model. Therefore, the model-update vector becomes

$$\mathbf{\Delta\lambda} = \{\Delta V^c_{P0}, \Delta\varepsilon^{(n)}, \Delta\delta^{(n)}\}, \quad (c = 1, 2, \ldots, W), \quad (n = 2, 3), \tag{13}$$

where W is the number of grid points in the model ($W = 81 \times 51$); $\varepsilon^{(1)}$ and $\delta^{(1)}$ in the top layer are still fixed at zero.

To solve the tomographic inverse problem, equation 2 is modified as

$$\mathcal{F}(\mathbf{\Delta\lambda}) = \|\mathbf{AC}\,\mathbf{\Delta\lambda} + \mathbf{b}\|^2 + \zeta_1^2\,\|\mathbf{C}\,\mathbf{\Delta\lambda}\|^2 + \zeta_2^2\,\|\mathbf{L}(\mathbf{\Delta\lambda} + \boldsymbol{\lambda}^{\mathbf{0}})\|^2, \tag{14}$$

where $\mathbf{C}$ is a mapping matrix similar to the one in equation 12, and the regularization term (with the same matrix $\mathbf{L}$ as in equation 2) is applied to smooth the velocity field in the process of flattening CIGs. Here, because the matrix $\mathbf{L}$ is a finite-difference approximation of the Laplacian operator, only parameter variations between adjacent grid points are restricted. Therefore, equation 14 can be used to recover nonlinear velocity fields, while in test 1 the spatial variation of V_{P0} was held linear. The parameter $\varepsilon^{(n)}$ is kept nonnegative, which is a plausible constraint for sedimentary rocks.

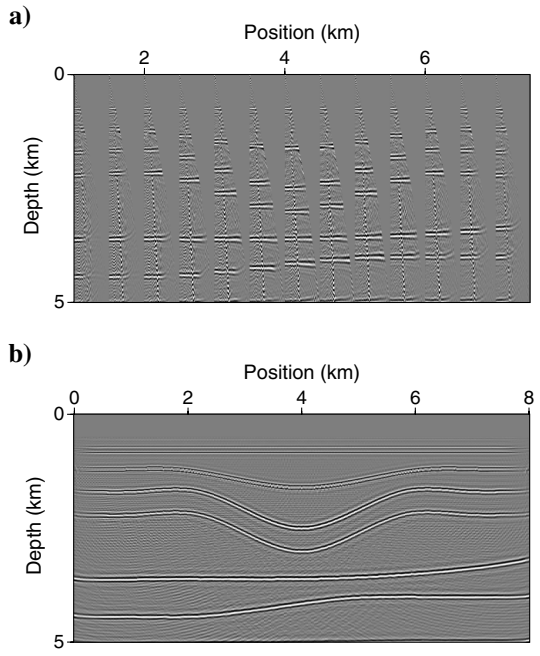

Figure 6. (a) CIGs after PSDM with the inverted parameters (Table 1) and (b) the corresponding depth image.

To build an initial isotropic model, we use the Dix-derived values of V_{nmo} from a common-midpoint (CMP) gather in the area with relatively flat reflectors (close to the left edge of the model). Then, the initial velocity field is obtained by image-guided interpolation (Hale, 2009) (Figure 7a). After 10 iterations, the residual moveout in the CIGs is largely removed (Figure 8a). On the final image (Figure 8b), the middle sections of the reflectors in the top two layers are well positioned (errors are up to ±80 m), but the two bottom reflectors and the interface segments near the model edges are somewhat distorted.

Because the symmetry-direction velocity V_{P0} is estimated on the grid, specifying it at any single point does not help in the inversion. Without a strong smoothing constraint (as the one in test 1), the velocity V_{P0} is obtained with substantial errors. In some areas of the top two layers, flattening the CIGs yields V_{P0} with accuracy higher than 5% (Figures 9a and 10a). The errors in V_{P0}, however, are much larger in the top left part of the model and in the section below the syncline. Moreover, because the velocity across the layer boundaries is discontinuous (Figure 3a), whereas the inversion

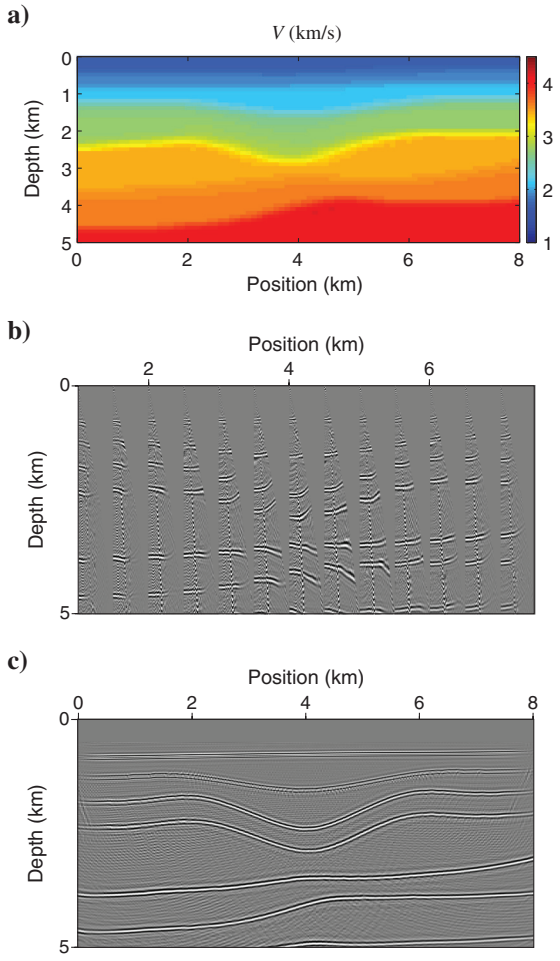

Figure 7. (a) Isotropic model for the first iteration of velocity analysis in test 2. The velocity is defined at each vertex of the 100 m ×100 m grid. There is substantial residual moveout in the CIGs which are displayed every 0.5 km from 1 km to 7 km on plot (b), and the depth image (c) is distorted.

operates with a smoothed model (equation 14), V_{P0} is distorted near the interfaces.

Because ε and δ were correctly assumed to be constant in each layer, both parameters are well-resolved (Figure 9b and 9c). To avoid inconsistent updates of ε and δ caused by interface movement at each iteration, we applied vertical smoothing over a distance of 100 m. As a result, there are no jumps in the inverted values of ε and δ across the boundaries. The velocities $V_h = V_{P0}\sqrt{1+2\varepsilon}$ and $V_{nmo} = V_{P0}\sqrt{1+2\delta}$, computed with the estimated parameters V_{P0}, ε, and δ, are distorted by less than 5% in the top two layers, except for the vicinity of the layer boundaries (Figure 10b and 10c). However, V_h and V_{nmo} below the syncline are poorly constrained, with errors up to 8%.

Test 3

The nonuniqueness of parameter estimation in anisotropic media is often reduced by including additional information, such as borehole data (Sexton and Williamson, 1998; Morice et al., 2004; Bakulin et al., 2010b). Therefore, in the next test we combine the surface reflection data with P-wave walkaway VSP traveltimes.

The parameters ε and δ are still assumed to be constant in each layer, but the number of layers is doubled to increase the complexity of the trial model and make it more realistic (i.e., each of the three layers is divided into two by an additional interface). Therefore, the model-update vector becomes

$$\Delta\boldsymbol{\lambda} = \{\Delta V_{P0}^{c}, \Delta\varepsilon^{(n)}, \Delta\delta^{(n)}\}, \quad (c = 1, 2, \ldots, W), \quad (n = 1, 2, \ldots, 6), \qquad (15)$$

where $W = 81 \times 51$ is the same as in test 2. Because the constraints from walkaway VSP data allow us to resolve all three TTI parameters, each layer is treated as anisotropic with the parameters V_{P0}^{c}, $\varepsilon^{(n)}$, and $\delta^{(n)}$ updated simultaneously.

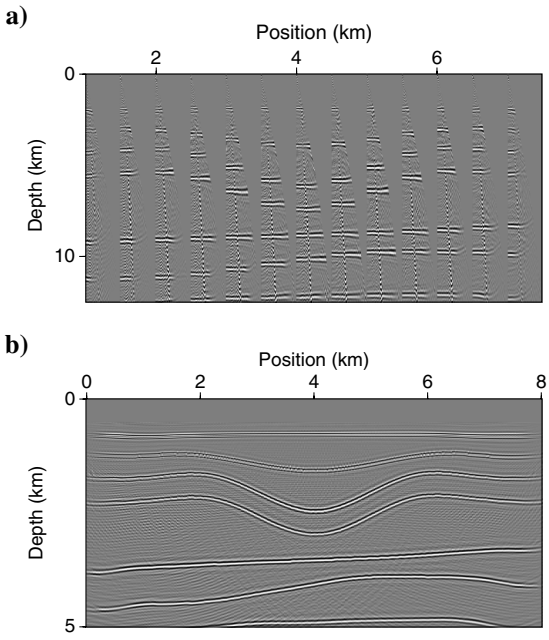

Figure 8. (a) CIGs after 10 iterations and (b) the corresponding depth image in test 2.

To generate synthetic VSP data, a vertical "well" is placed at location $x_{VSP} = 3$ km, with a string of 46 receivers spanning the depth interval from 0.09 km to 4.59 km every 100 m. The sources are located at the surface between $x = 0.05$ km and $x = 5.95$ km, also with an interval of 100 m. The traveltime t_{VSP} for each source-receiver pair is obtained by ray tracing in the actual model (Figure 3).

During the iterative inversion, VSP traveltimes t_{VSP}^{calc} are computed by anisotropic ray tracing for each trial model. The difference between the observed and calculated traveltimes $\mathbf{d} = t_{VSP} - t_{VSP}^{calc}$ can serve as the input to traveltime tomography (Chapman and Pratt, 1992; Pratt and Chapman, 1992) based on the following equation

$$\mathbf{EC}\,\Delta\boldsymbol{\lambda} = \mathbf{d}. \qquad (16)$$

The matrix $\mathbf{E}$ is composed of the traveltime derivatives with respect to the parameters at each grid point, and the matrix $\mathbf{C}$ plays the same role as that in equation 12 — it maps the model update $\Delta\boldsymbol{\lambda}$ into the parameter perturbation at each grid point. To solve the joint tomographic inverse problem, we minimize the function

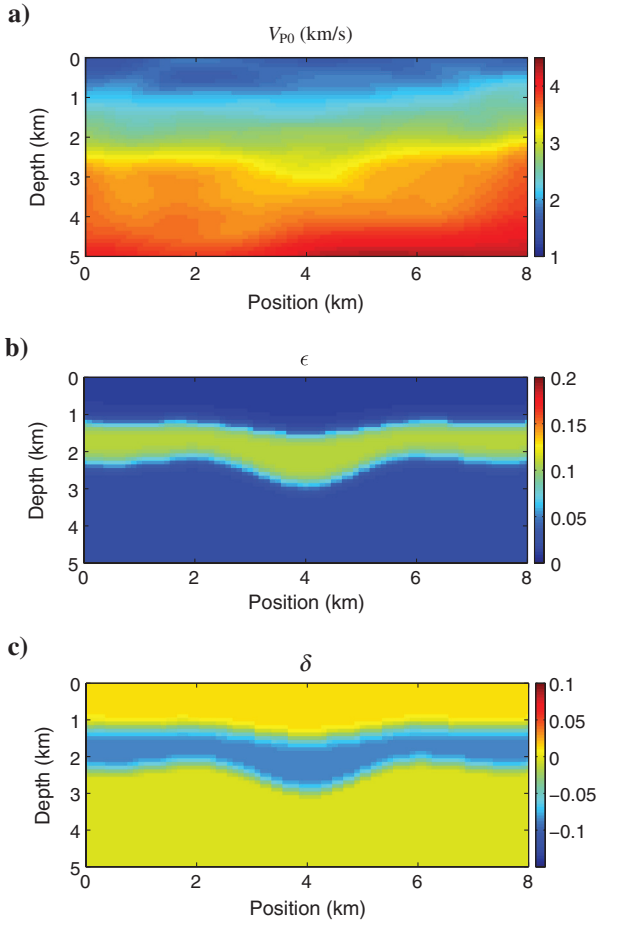

Figure 9. (a) Symmetry-direction velocity V_{P0} estimated at each grid point in test 2. The inverted interval parameters (b) ε and (c) δ. Vertical smoothing over a distance of 100 m was applied

$$\mathcal{F}(\Delta\boldsymbol{\lambda}) = \|\mathbf{AC}\,\Delta\boldsymbol{\lambda} + \mathbf{b}\|^2 + \zeta_{\mathrm{VSP}}^2\|\mathbf{EC}\,\Delta\boldsymbol{\lambda} - \mathbf{d}\|^2 + \zeta_1^2\,\|\mathbf{C}\,\Delta\boldsymbol{\lambda}\|^2 + \zeta_2^2\,\|\mathbf{L}(\Delta\boldsymbol{\lambda} + \boldsymbol{\lambda}^{\mathbf{0}})\|^2, \qquad (17)$$

where ζ_{VSP} is the weighting factor of the VSP traveltime misfit.

If borehole information is available, it is possible to build an initial TTI velocity model using, for example, stacking-velocity tomography (Wang and Tsvankin, 2010). Here, to ensure consistency, we use the same isotropic initial model as that in test 2. The VSP data are directly used in the iterative tomographic algorithm to constrain the anisotropic velocity field.

After 15 iterations, the tomographic inversion significantly reduced the misfit of VSP traveltimes (Figure 11b). Also, CIGs are flat throughout much of the model (Figures 11a and 12a), although several gathers close to the right edge still exhibit apparent RMO because VSP data do not provide constraints on the right side of the section. The reflectors on the final image (Figure 12b) are accurately positioned (errors are up to ±50 m), with somewhat larger distortions near the edges due to errors in the velocity field.

With the constraints from VSP data, the spatially varying symmetry-direction velocity V_{P0} is well-recovered (Figure 13a), with absolute errors in most areas smaller than 2% (Figure 14a).

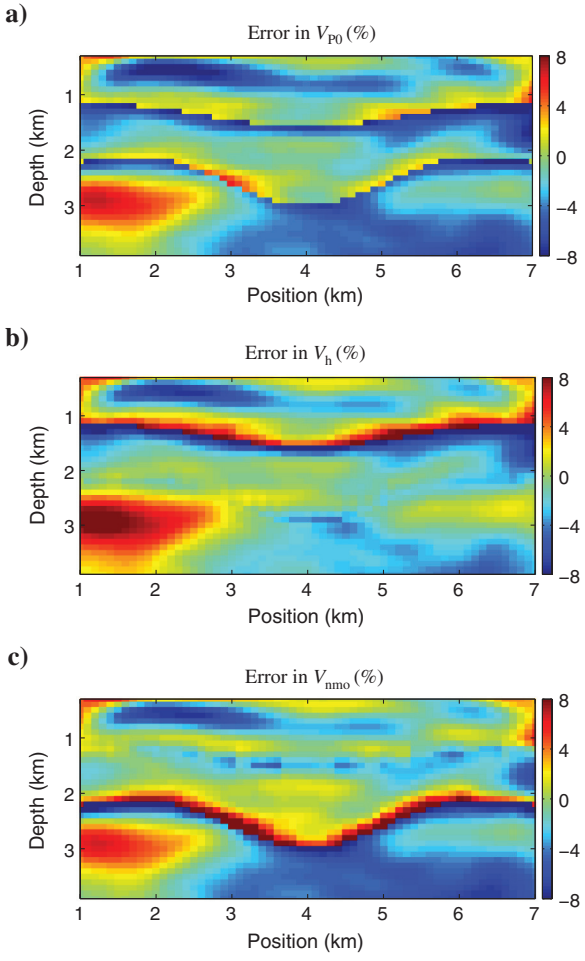

Figure 10. Percentage velocity errors in test 2 for 1 km ≤ x ≤ 7 km and 0.3 km ≤ z ≤ 3.9 km. (a) V_{P0}, (b) V_h, and (c) V_{nmo}.

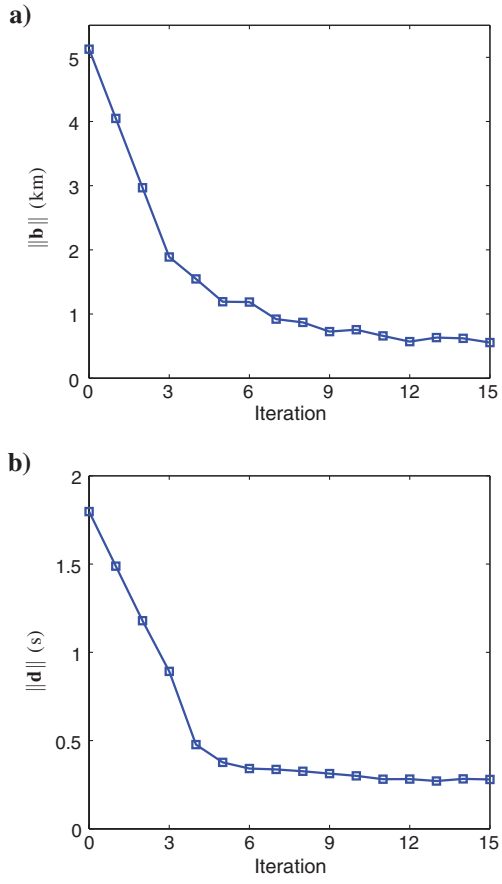

Figure 11. (a) L^2-norm of the residual moveout in CIGs at each iteration for joint inversion of reflection and VSP data (test 3, equation 17). (b) The L^2-norm of the VSP traveltime misfit in equation 17.

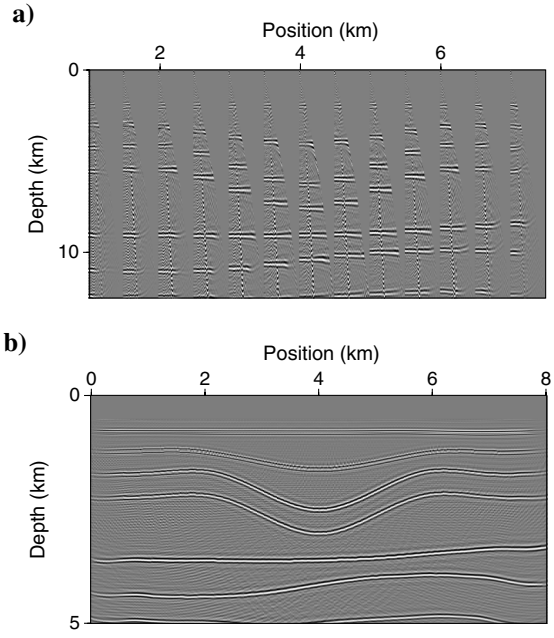

Figure 12. (a) CIGs after 15 iterations and (b) the corresponding depth image in test 3. There is residual moveout ("hockey sticks") at long offsets for events near both edges of the model.

As in test 2, the errors in V_{P0} are higher near the layer boundaries (Figure 14a). Due to the insufficient angle coverage of both reflection and VSP data, the errors in ε and δ in the bottom layer increase up to 0.05 (Figure 13b and 13c). The velocities V_h and V_{nmo} are generally distorted by less than 3% (Figure 14b and 14c), although the errors at grid points near the layer boundaries are somewhat larger.

TTI thrust sheet

Next, we test the algorithm on the synthetic data of Zhu et al. (2007), whose model (simulating typical structures in the Canadian Foothills) includes a TTI thrust sheet embedded in an otherwise isotropic, homogeneous medium (Figure 15). P-wave reflection data are generated by anisotropic finite-difference modeling. The sources and receivers used in our test are placed every 60 m with the maximum offset reaching 1980 m. Because the exact model geometry (i.e., interface positions) is unavailable, we cannot provide comparisons of our migration results with the actual section.

The initial model for MVA includes two horizontal isotropic layers (Figure 16a). Although the P-wave velocity in the isotropic background is set to the correct value, ignoring transverse isotropy causes noticeable RMO in CIGs (Figure 16b) and a strong distortion of the imaged reflector beneath the thrust sheet (Figure 16c).

In the model-updating process, the velocity V_{P0} is defined on a square (100 m × 100 m) grid. Based on the picked reflectors, the model is divided into two isotropic blocks and a TTI layer sandwiched between them. Within each layer/block, the anisotropy parameters ε and δ are assumed to be constant. The symmetry axis is taken perpendicular to the reflectors, with the tilt changing during the updates. Because there is only a single deep horizontal reflector on the right side of the model (Figure 15), the parameters ε and δ cannot be resolved solely from P-wave reflection data. Therefore, both ε and δ in the block to the right of the TTI layer are set to zero.

After 12 iterations using the objective function in equation 14, the velocity in the TTI layer is partially recovered (Figure 17a). Because V_{P0} is updated on a relatively fine grid, flattening the CIGs along three reflectors (only one reflector for the block on the right side) with general smoothing regularization (equation 14) is insufficient to recover the velocity field. For example, there is noticeable heterogeneity in each block that does not exist in the actual model. With the constraints provided by a wide range of dips in the TTI thrust sheet and the correct assumption about the spatial variation of ε and δ, both parameters inside the sheet are well resolved

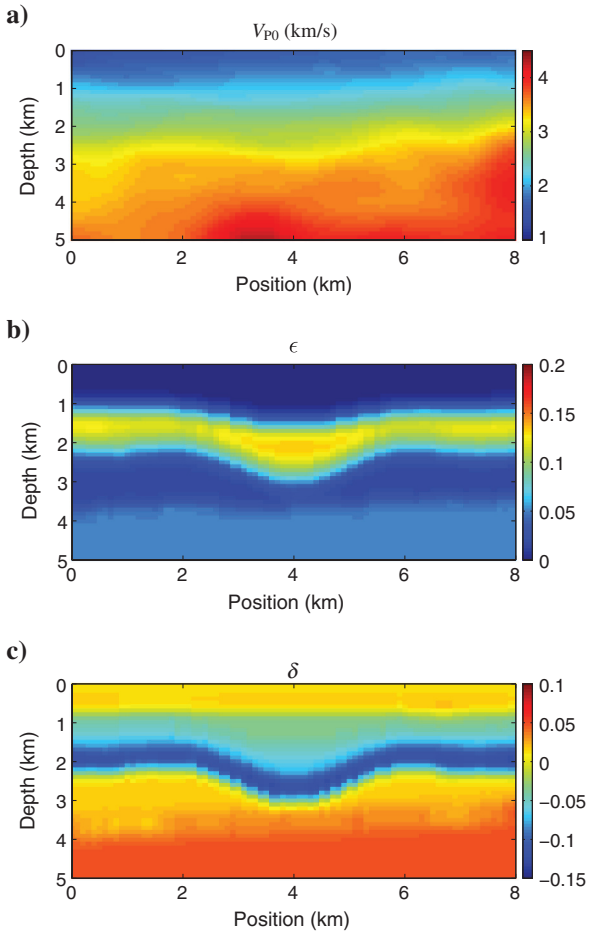

Figure 13. (a) Symmetry-direction velocity V_{P0} estimated at each grid point in test 3. (b, c) The inverted layer-based parameters ε and δ (the model includes six layers instead of three in test 2).

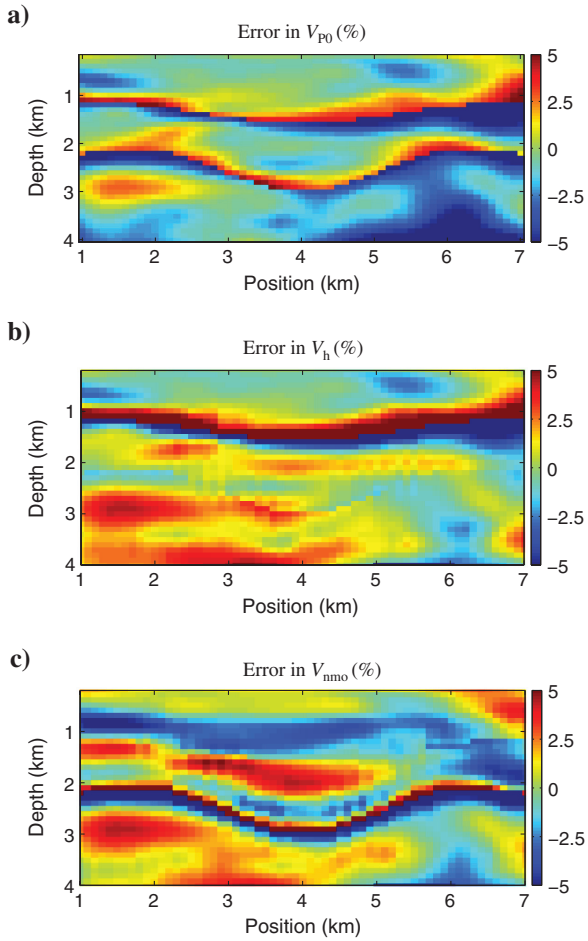

Figure 14. Percentage velocity errors in test 3 for 1 km ≤ x ≤ 7 km and 0.2 km ≤ z ≤ 4 km. (a) V_{P0}, (b) V_h, and (c) V_{nmo}.

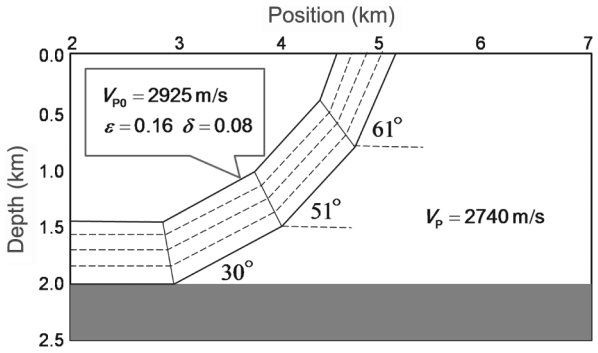

Figure 15. Schematic plot of the synthetic model from Zhu et al. (2007) (exact model geometry is unknown). The bending thrust sheet is TTI with the symmetry axis perpendicular to the boundaries. The dips range from 0° to 61°, and the interval parameters of the sheet are $V_{P0} = 2925$ m/s, $\varepsilon = 0.16$, and $\delta = 0.08$. The P-wave velocity in the isotropic background medium is 2740 m/s.

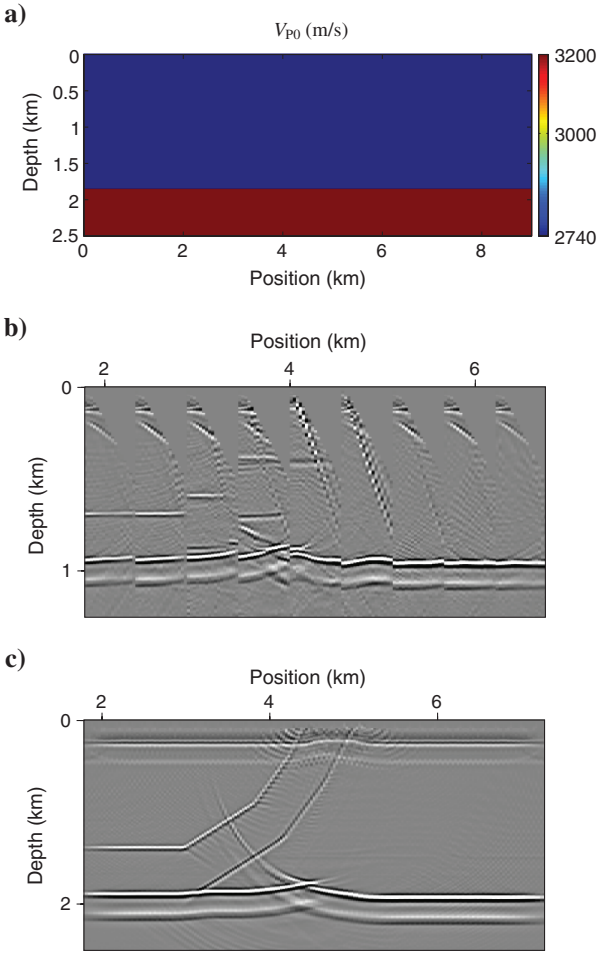

Figure 16. (a) Initial isotropic model used in velocity analysis for the model from Figure 15. The P-wave velocities in the top and bottom layers are 2740 m/s and 3200 m/s, respectively. (b) The CIGs computed with the initial model and displayed every 0.6 km. (c) The corresponding depth image.

(Figure 17b and 17c). The error in ε in the TTI layer (0.03) is somewhat larger than that in $\delta\,(-0.01)$ because of the small offset-to-depth ratio, which is close to unity for the bottom reflector. Despite remaining distortions in V_{P0}, the obtained anisotropic velocity field largely removes the residual moveout in the CIGs (Figure 18a) and improves the depth image, especially that of the bottom horizontal reflector (Figure 18b). Additional reflectors or walkaway VSP data would allow us to improve reconstruction of the velocity field.

DISCUSSION

Here, we assumed the symmetry axis to be perpendicular to the reflectors. This common assumption not only stabilizes parameter estimation, but also simplifies ray tracing because the incidence and reflection angles are equal. In reality, however, the symmetry axis may not be aligned with the reflector normal if, for example, sedimentation and tectonic processes occur simultaneously (Bakulin et al., 2010b). Also, in sediments near salt bodies, stress-induced anisotropy may cause deviation of the symmetry axis from the normal to the bedding. Sometimes, the symmetry-axis orientation may be constrained using a priori information (e.g., geologic data), which may help express the tilt ν as a function of reflector dip. Otherwise, an unknown direction of the symmetry axis significantly

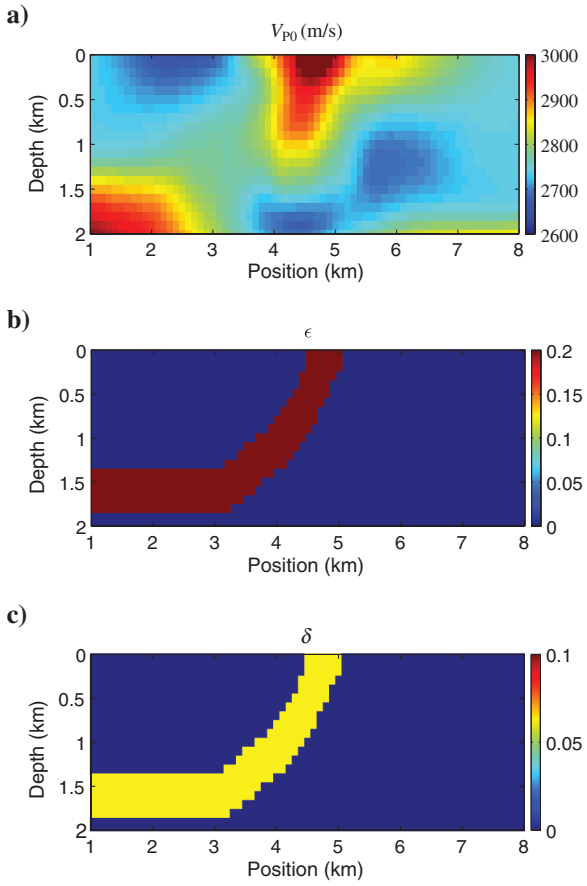

Figure 17. (a) Symmetry-direction velocity V_{P0} estimated at each grid point. The inverted block-based parameters (b) ε and (c) δ. In the TTI layer, the estimated $\varepsilon = 0.19$ and $\delta = 0.07$. The parameters ε and δ in the block to the right of the TTI layer are set to zero.

increases the nonuniqueness of the inversion. Note that, except for the need to compute the reflection angle from Snell's law, deviation of the symmetry axis from the reflector normal does not require substantial changes in the tomographic algorithm.

In areas with sufficient ray coverage, higher model resolution can be achieved with smaller grids. In general, resolution depends on many factors, such as acquisition geometry, seismic frequency, and complexity of subsurface structures (Woodward et al., 2008). For example, spatial resolution typically decreases with depth because of a larger Fresnel zone and insufficient constraints provided by deep reflection events. Below salt bodies, resolution is also reduced because of illumination problems. Therefore, uniform rectangular/square grids used here may not be optimal in practice. To obtain a better velocity model, grid points can be distributed according to the ray density, size of the Fresnel zone, and geologic information. Then, it may be convenient to divide the model into triangular (2D) or tetrahedral (3D) cells of different size (Fomel and Guitton, 2006; Lelièvre et al., 2012).

Here, we employed Tikhonov (1963) regularization to smooth the velocity field in both horizontal and vertical directions. Clapp et al. (2004) develop so-called "steering filters" designed to steer the velocity variations according to geologic structures (e.g., layers). Using the steering-filter preconditioner, Bakulin et al. (2010c) perform joint tomographic inversion of P-wave reflection data and check-shot traveltimes for VTI media. In a sequel paper, we introduce similar regularization terms that smooth the model parameters along layer boundaries, while allowing for more pronounced variations in the orthogonal direction. Such "structure-guided" regularization may provide useful geologic constraints in field applications of MVA.

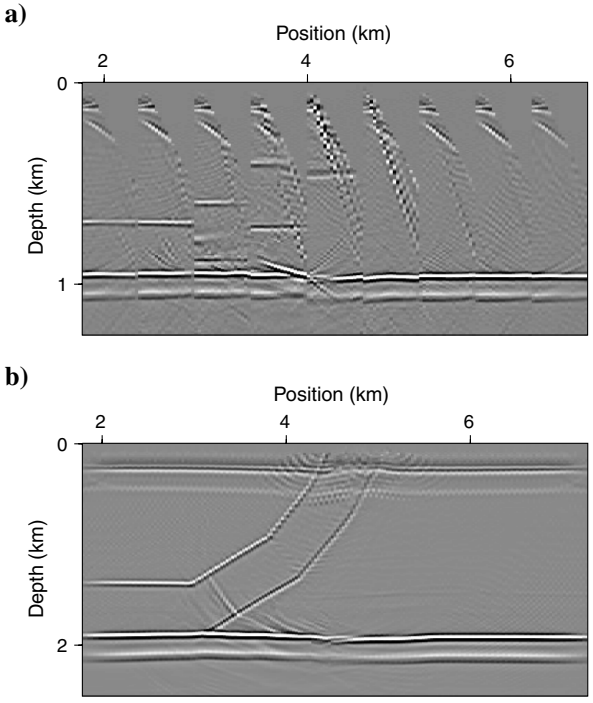

Figure 18. (a) CIGs after 12 iterations and (b) the corresponding depth image. Note that the reflector beneath the thrust sheet has been flattened.

CONCLUSIONS

Currently TTI models are often used to improve imaging results in complex geologic environments including subsalt plays and active tectonic areas (e.g., the Canadian Foothills). However, allowing for the tilt of the symmetry axis introduces additional uncertainty into estimation of the interval TTI parameters, even if the symmetry-axis orientation is fixed using a priori information. Here, we developed efficient 2D reflection tomography for TTI models, with the parameters V_{P0}, ε, δ, and the symmetry-axis tilt ν defined on a rectangular grid. To remove residual moveout of reflection events in CIGs, migrated depths are described by a nonhyperbolic equation that remains accurate for large offsets.

Model updating is performed by iterative linearized inversion for V_{P0}, ε, and δ, while the spatial distribution of ν is obtained by setting the symmetry axis orthogonal to the reflectors. The Fréchet matrix at each iteration is constructed by approximately evaluating the traveltime derivatives with respect to the TTI parameters at all grid points near the reflection raypaths. The devised algorithm is used to explore the influence of different assumptions about the spatial variation of TTI parameters on the accuracy of the inverted model.

Numerical testing is first performed for a three-layer medium with a quasi-factorized TTI syncline (in which ε and δ are constant) embedded between isotropic layers with linear velocity variation. The symmetry-direction velocity V_{P0} in the TTI layer also varies linearly, while the symmetry axis is orthogonal to the layer boundaries. With several correct model assumptions (i.e., if ε and δ are known to be constant in each layer, the interval velocity is defined by the vertical and lateral gradients, and the first layer is treated as isotropic), the algorithm accurately reconstructs the velocity field with no other a priori information. If V_{P0} is updated separately at each grid point while the anisotropy parameters are still assumed to be constant in each layer, flattening the CIGs helps recover the velocities $V_h = V_{P0}\sqrt{1+2\varepsilon}$ and $V_{nmo} = V_{P0}\sqrt{1+2\delta}$ in the first two layers with errors reaching 5%. The accuracy of the inverted velocities is lower in the layer below the TTI syncline.

In another test for the same model, reflection data are combined with P-wave walkaway VSP traveltimes. While V_{P0} is updated at each grid point, ε and δ are taken constant in six "sublayers" (each layer was divided into two). Because of the additional constraints from VSP data, the velocities V_{P0}, V_h, and V_{nmo} are well-resolved (errors are smaller than 3%) for most of the model, and the errors in ε and δ do not exceed 0.02 (except for the bottom layer).

The other synthetic model includes a bending TTI thrust sheet with constant parameters ε and δ. The velocity V_{P0} is updated on a grid, while the quasi-factorized assumption proves sufficient to recover both ε and δ due to a wide range of reflector dips. Without walkaway VSP traveltimes, however, the velocity V_{P0} in each layer cannot be resolved just by flattening the CIGs for the available three reflectors, despite application of general smoothing regularization.

ACKNOWLEDGMENTS

We are grateful to CWP alumni Debashish Sarkar (GXT), Zhenyue Liu (ExxonMobil), and Tariq Alkhalifah (KAUST, Saudi Arabia) for significant contributions to Seismic Unix, which serves as the platform for our software development. We also thank Sam Gray (CGGVeritas) for providing the data for the second synthetic example, and Mirko van der Baan, Sam Gray, Ivan Pšenčík, and two anonymous referees for their reviews of the manuscript. X. Wang

would like to thank Zhaobo Meng (In-Depth Geo) for his help and advice during an internship with ConocoPhillips in 2009. This work was supported by the Consortium Project on Seismic Inverse Methods for Complex Structures at the Center for Wave Phenomena.

APPENDIX A

PARAMETER-UPDATING METHODOLOGY

Here, the MVA algorithm for factorized VTI media introduced by Sarkar and Tsvankin (2004) is extended to gridded TTI models. To linearize the velocity-analysis problem, we employ an iterative technique based on the following updating procedure.

Suppose that after the $(l-1)$th iteration of MVA, PSDM produces the migrated depths $z_0(x_j, h_k)$ (x_j is the midpoint of the jth image gather, and h_k is the half-offset). The migrated depths $z(x_j, h_k)$ after the lth iteration can be expressed as a linear perturbation of $z_0(x_j, h_k)$:

$$z(x_j, h_k) = z_0(x_j, h_k) + \sum_{c=1}^{W}\sum_{i=1}^{N} \frac{\partial z_0(x_j, h_k)}{\partial \lambda_{ic}}\,\Delta\lambda_{ic}, \quad \text{(A-1)}$$

where W is the number of grid points ($c = 1, 2, \ldots, W$), $\partial z_0(x_j, h_k)/\partial\lambda_{ic}$ are the derivatives of the migrated depths with respect to the medium parameters λ_i ($i = 1, 2, \ldots, N$) at the vertex c, and $\Delta\lambda_{ic} = \lambda_{ic} - \lambda_{ic}^0$ are the desired parameter updates. Note that $\partial z_0(x_j, h_k)/\partial\lambda_{ic} = 0$, if a specific ray does not cross any cell with the vertex c (a vertex is shared by four cells). After obtaining the update $\Delta\lambda_{ic}$, we can find the parameters λ_{ic} for the next (lth) iteration of PSDM.

Following the MVA algorithm of Liu (1997), Sarkar and Tsvankin (2004) define the variance of the migrated depths for all offsets and image gathers as

$$\text{Var} = \sum_{j=1}^{P}\sum_{k=1}^{M} [z(x_j, h_k) - \hat{z}(x_j)]^2, \quad \text{(A-2)}$$

where $\hat{z}(x_j) = (1/M)\sum_{k=1}^{M} z(x_j, h_k)$ is the average migrated depth of a reflection event at midpoint x_j, P is the number of image gathers, and M is the number of offsets in each image gather. At each iteration, the goal is to find the parameter updates that make the derivative of Var with respect to $\Delta\lambda_{rs}$ ($r = 1, 2, \ldots, N$, and $s = 1, 2, \ldots, W$) vanish, which helps minimize the RMO in all CIGs. Using equations A-1 and A-2, we can differentiate the variance Var with respect to the updates and set $\partial\text{Var}/\partial(\Delta\lambda_{rs}) = 0$, which yields an equation for $\Delta\lambda_{ic}$:

$$\sum_{j=1}^{P}\sum_{k=1}^{M}\sum_{c=1}^{W}\sum_{i=1}^{N}(g_{jk,ic} - \hat{g}_{j,ic})(g_{jk,rs} - \hat{g}_{j,rs})\,\Delta\lambda_{ic} = -\sum_{j=1}^{P}\sum_{k=1}^{M}[z_0(x_j, h_k) - \hat{z}_0(x_j)](g_{jk,rs} - \hat{g}_{j,rs}), \quad \text{(A-3)}$$

where $g_{jk,ic} \equiv \partial z_0(x_j, h_k)/\partial\lambda_{ic}$ (the subscripts r and s correspond to i and c, respectively), and $\hat{g}_{j,ic} = (1/M)\sum_{k=1}^{M} g_{jk,ic}$. Equation A-3 can be rewritten in matrix form as

$$\mathbf{A}^T\mathbf{A}\,\Delta\boldsymbol{\lambda} = -\mathbf{A}^T\mathbf{b}, \quad \text{(A-4)}$$

where the matrix $\mathbf{A}$ has $M \times P$ rows and $W \times N$ columns (its elements are $g_{jk,ic} - \hat{g}_{j,ic}$); the superscript $\mathbf{T}$ denotes the transpose, and $\mathbf{b}$ is a vector with $M \times P$ elements defined as $z_0(x_j, h_k) - \hat{z}_0(x_j)$.

To evaluate the derivatives of the migrated depths $z(x_j, h_k)$ for a gridded model, we modify the function given by Sarkar and Tsvankin (2004) as

$$\frac{dz}{d\lambda_{ic}} = -\left[\frac{\partial\tau_s}{\partial\lambda_{ic}} + \frac{\partial\tau_r}{\partial\lambda_{ic}}\right]\frac{1}{q_s + q_r}, \quad \text{(A-5)}$$

where τ_s is the traveltime from the source to the reflector obtained after PSDM with the medium parameters λ_{ic}^0, τ_r is the traveltime from the reflector to the receiver, and $q_s = \partial\tau_s/\partial z$ and $q_r = \partial\tau_r/\partial z$ are the vertical slownesses at the reflector for the rays connecting the reflection point with the source and receiver, respectively. Equation A-5 expresses $\partial z(x_j, h_k)/\partial\lambda_{ic}$ through the traveltime derivatives and vertical slownesses — quantities that can be computed from anisotropic ray tracing.

REFERENCES

Alkhalifah, T., 1995, Efficient synthetic-seismogram generation in transversely isotropic, inhomogeneous media: Geophysics, **60**, 1139–1150, doi: 10.1190/1.1443842.

Alkhalifah, T., and K. Larner, 1994, Migration error in transversely isotropic media: Geophysics, **59**, 1405–1418, doi: 10.1190/1.1443698.

Alkhalifah, T., I. Tsvankin, K. Larner, and J. Toldi, 1996, Velocity analysis and imaging in transversely isotropic media: Methodology and a case study: The Leading Edge, **15**, 371–378, doi: 10.1190/1.1437345.

Audebert, F., A. Pettenati, and V. Dirks, 2006, TTI anisotropic depth migration — Which tilt estimate should we use?: EAGE Expanded Abstracts, 185–190.

Bakulin, A., Y. Liu, O. Zdraveva, and K. Lyons, 2010a, Anisotropic model building with wells and horizons: Gulf of Mexico case study comparing different approaches: The Leading Edge, **29**, 1450–1460, doi: 10.1190/1.3525359.

Bakulin, A., M. Woodward, D. Nichols, K. Osypov, and O. Zdraveva, 2010b, Building tilted transversely isotropic depth models using localized anisotropic tomography with well information: Geophysics, **75**, no. 4, D27–D36, doi: 10.1190/1.3453416.

Bakulin, A., M. Woodward, O. Zdraveva, and D. Nichols, 2010c, Application of steering filters to localized anisotropic tomography with well data: 80th Annual International Meeting, SEG, Expanded Abstracts, 4286–4290.

Behera, L., and I. Tsvankin, 2009, Migration velocity analysis for tilted transversely isotropic media: Geophysical Prospecting, **57**, 13–26, doi: 10.1111/j.1365-2478.2008.00732.x.

Berkhout, A., 1982, Seismic migration — Imaging of acoustic energy by wavefield extrapolation: Elsevier Scientific Publishing Company.

Campbell, A., E. Evans, D. Judd, I. Jones, and S. Elam, 2006, Hybrid gridded tomography in the southern North Sea: 76th Annual International Meeting, SEG, Expanded Abstracts, 2538–2541.

Červený, V., 2001, Seismic ray theory: Cambridge University Press.

Červený, V., and J. Jech, 1982, Linearized solutions of kinematic problems of seismic body waves in inhomogeneous slightly anisotropic media: Journal of Geophysics, **51**, 96–104.

Chapman, C. H., and R. G. Pratt, 1992, Traveltime tomography in anisotropic media — I. Theory: Geophysical Journal International, **109**, 1–19, doi: 10.1111/j.1365-246X.1992.tb00075.x.

Charles, S., D. Mitchell, R. Holt, J. Lin, and J. Mathewson, 2008, Data-driven tomographic velocity analysis in tilted transversely isotropic media: A 3D case history from the Canadian Foothills: Geophysics, **73**, no. 5, VE261–VE268, doi: 10.1190/1.2952915.

Clapp, R. G., B. L. Biondi, and J. F. Claerbout, 2004, Incorporating geologic information into reflection tomography: Geophysics, **69**, 533–546, doi: 10.1190/1.1707073.

Coleman, T. F., and Y. Li, 1996, A reflective Newton method for minimizing a quadratic function subject to bounds on some of the variables: SIAM Journal on Optimization, **6**, 1040–1058, doi: 10.1137/S1052623494240456.

Deregowski, S. M., 1990, Common-offset migrations and velocity analysis: First Break, **8**, 225–234.

Douma, J., R. Frijhof, B. Hewett, M. Jacobi, M. Kohli, L. Lepre, C. Perkins, M. McRae, J. Razzano, E. Salo, and A. Stopin, 2009, Seismic processing

for GOM development projects — Business impact of anisotropy: 79th Annual International Meeting, SEG, Expanded Abstracts, 3476–3481.
Etgen, J., 1988, Velocity analysis using prestack depth migration: Linear theory: 58th Annual International Meeting, SEG, Expanded Abstracts, 909–912.
Etgen, J., 1990, Residual prestack migration and interval-velocity estimation: Ph.D. thesis, Stanford University.
Fomel, S., and A. Guitton, 2006, Regularizing seismic inverse problems by model reparameterization using plane-wave construction: Geophysics, **71**, no. 5, A43–A47, doi: 10.1190/1.2335609.
Fowler, P., 1988, Migration velocity analysis: Ph.D. thesis, Stanford University.
Fowler, P., 2003, Practical VTI approximations: a systematic anatomy: Journal of Applied Geophysics, **54**, 347–367, doi: 10.1016/j.jappgeo.2002.12.002.
Gill, P. E., W. Murray, and M. H. Wright, 1981, Practical optimization: Academic Press.
Hale, D., 2009, Image-guided blended neighbor interpolation of scattered data: 79th Annual International Meeting, SEG, Expanded Abstracts, 1127–1131.
Huang, T., S. Xu, J. Wang, G. Ionescu, and M. Richardson, 2008, The benefit of TTI tomography for dual azimuth data in Gulf of Mexico: 78th Annual International Meeting, SEG, Expanded Abstracts, 222–226.
Jech, J., and I. Pšenčík, 1992, Kinematic inversion for qP- and qS-waves in inhomogeneous hexagonally symmetric structures: Geophysical Journal International, **108**, 604–612, doi: 10.1111/j.1365-246X.1992.tb04639.x.
Lelièvre, P., A. Carter-McAuslan, C. Farquharson, and C. Hurich, 2012, Unified geophysical and geological 3D Earth models: The Leading Edge, **31**, 322–328, doi: 10.1190/1.3694900.
Liu, Z., 1997, An analytical approach to migration velocity analysis: Geophysics, **62**, 1238–1249, doi: 10.1190/1.1444225.
Lumley, D. E., 1989, Kirchhoff prestack depth migration: Imaging conditions and amplitude recovery: 59th Annual International Meeting, SEG, Expanded Abstracts, 1336–1339.
Morice, S., J.-C. Puech, and S. Leaney, 2004, Well-driven seismic: 3D data processing solutions from wireline logs and borehole seismic data: First Break, **22**, 61–66.
Murphy, G., and S. Gray, 1999, Manual seismic reflection tomography: Geophysics, **64**, 1546–1552, doi: 10.1190/1.1444658.
Neal, S., N. R. Hill, and Y. Wang, 2009, Anisotropic velocity modeling and prestack Gaussian-beam depth migration with applications in the deepwater Gulf of Mexico: The Leading Edge, **28**, 1110–1119, doi: 10.1190/1.3236381.
Pratt, R. G., and C. H. Chapman, 1992, Traveltime tomography in anisotropic media — II. Applications: Geophysical Journal International, **109**, 20–37, doi: 10.1111/j.1365-246X.1992.tb00076.x.
Sarkar, D., and I. Tsvankin, 2004, Migration velocity analysis in factorized VTI media: Geophysics, **69**, 708–718, doi: 10.1190/1.1759457.
Sexton, P., and P. Williamson, 1998, 3D anisotropic velocity estimation by model-based inversion of pre-stack traveltimes: 68th Annual International Meeting, SEG, Expanded Abstracts, 1855–1858.
Stork, C., 1992, Reflection tomography in the postmigrated domain: Geophysics, **57**, 680–692, doi: 10.1190/1.1443282.
Tikhonov, A. N., 1963, Solution of incorrectly formulated problems and the regularization method: Soviet Mathematics Doklady, **4**, 1035–1038.
Tsvankin, I., 1996, P-wave signatures and notation for transversely isotropic media: An overview: Geophysics, **61**, 467–483, doi: 10.1190/1.1443974.
Tsvankin, I., 2005, Seismic signatures and analysis of reflection data in anisotropic media (second edition): Elsevier Scientific Publishing Company.
Tsvankin, I., and V. Grechka, 2011, Seismology of azimuthally anisotropic media and seismic fracture characterization: Society of Exploration Geophysicists.
van Trier, J., 1990, Tomographic determination of structural velocities from depth-migrated seismic data: Ph.D. thesis, Stanford University.
Vestrum, R., D. Lawton, and R. Schmid, 1999, Imaging structures below dipping TI media: Geophysics, **64**, 1239–1246, doi: 10.1190/1.1444630.
Wang, X., and I. Tsvankin, 2010, Stacking-velocity inversion with borehole constraints for tilted TI media: Geophysics, **75**, no. 5, D69–D77, doi: 10.1190/1.3481652.
Woodward, M. J., D. Nichols, O. Zdraveva, P. Whitfield, and T. Johns, 2008, A decade of tomography: Geophysics, **73**, no. 5, VE5–VE11, doi: 10.1190/1.2969907.
Zhou, B., and S. Greenhalgh, 2008, Non-linear traveltime inversion for 3-D seismic tomography in strongly anisotropic media: Geophysical Journal International, **172**, 383–394, doi: 10.1111/j.1365-246X.2007.03649.x.
Zhou, C., J. Jiao, S. Lin, J. Sherwood, and S. Brandsberg-Dahl, 2011, Multiparameter joint tomography for TTI model building: Geophysics, **76**, no. 5, WB183–WB190, doi: 10.1190/geo2010-0395.1.
Zhou, H., D. Pham, and S. Gray, 2004, Tomographic velocity analysis in strongly anisotropic TTI media: 74th Annual International Meeting, SEG, Expanded Abstracts, 2347–2351.
Zhu, T., S. Gray, and D. Wang, 2007, Prestack Gaussian-beam depth migration in anisotropic media: Geophysics, **72**, no. 3, S133–S138, doi: 10.1190/1.2711423.